Catalysis Science & Technology

PAPER

View Article Online
View Journal | View Issue

Cite this: *Catal. Sci. Technol.*, 2015, 5, 3166

Low-temperature CO oxidation on CuO/CeO_2 catalysts: the significant effect of copper precursor and calcination temperature

Shuaishuai Sun,[a] Dongsen Mao,*[a] Jun Yu,[a] Zhiqiang Yang,[a] Guanzhong Lu[a] and Zhen Ma[b]

Received 27th January 2015,
Accepted 16th March 2015

DOI: 10.1039/c5cy00124b

www.rsc.org/catalysis

CuO/CeO_2 catalysts for CO oxidation were prepared by impregnation using different Cu precursors (acetate, nitrate, chloride, and sulfate) and calcined at 500 or 800 °C. Their physicochemical properties were characterized by TG-DSC, XRD, TEM, N_2 adsorption, Raman, XPS, H_2-TPR, CO-TPD, and DRIFTS. The results show that CuO is the dominant Cu species in all cases except for copper sulfate calcined at 500 °C, under which temperature some $Cu_2(OH)_3Cl$ are also obtained from copper chloride. CuO/CeO_2 prepared from copper acetate and calcined at 500 °C shows the best activity for CO oxidation, due to the presence of more finely dispersed CuO and stronger synergistic effects. The synergistic effects can induce the formation of Cu^+ (the better CO adsorption sites) and activate the lattice oxygen, thus exerting a crucial role in the catalytic process. However, the residual Cl^- and SO_4^{2-} have a negative effect on the synergistic effects, resulting in low activity in CO oxidation.

1. Introduction

$CuO–CeO_2$ mixed oxides have attracted much attention recently because of their low costs, high catalytic activities, and wide applications in CO oxidation,[1–12] preferential CO oxidation in a H_2-rich stream,[13–17] partial oxidation of methane,[18] combustion of volatile organic compounds,[19,20] NO reduction by CO,[21] and water-gas shift reaction.[22,23] In particular, the activity of $CuO–CeO_2$ in CO oxidation can even be comparable to that of supported Pt catalysts.[1,3] CeO_2 with superior oxygen storage capacity can promote the dispersion and thermal stability of CuO, and can interact with CuO, thus changing their respective physicochemical properties.[1,5,6,10] It is generally recognized that the better dispersion of CuO and the strengthened synergistic effects can lead to higher catalytic activities in CO oxidation.[1,5,10,24]

Preparation methods have a significant influence on the particle size and dispersion of Cu species, as well as the $CuO–CeO_2$ interaction.[6,13,25,26] Methods used for the preparation of $CuO–CeO_2$ catalysts include impregnation,[1,2,4,8,12,13,24] co-precipitation,[6,13,22] sol–gel,[5,25] deposition–precipitation,[6] solvated metal atom impregnation,[27] inert gas condensation,[3] urea–nitrate combustion,[13,20] and hydrothermal synthesis.[28,29] Among them, impregnation is the most frequently used due to its simplicity, convenience, and high efficiency.[2,30] For instance, Luo *et al.*[2] reported that CuO/CeO_2 prepared by impregnation was more active than the one prepared by co-precipitation. Manzoli *et al.*[30] found that CuO/CeO_2 prepared by simple impregnation was as active as those prepared by more complex methods.

As catalytic behavior strongly depends on the preparation parameters, such as precursor, support, drying temperature/time, and calcination temperature/time, a detailed study of different factors is necessary. Attempts have been made to modify the CeO_2 support to make better catalysts. For example, Zheng *et al.*[8,31,32] synthesized a series of CeO_2 supports *via* sol–gel, alcohol-thermal, and thermal decomposition methods, and loaded CuO onto CeO_2 *via* impregnation. CeO_2 with smaller particle sizes, better crystallinity, and larger surface areas led to highly dispersed CuO responsible for high activity in CO oxidation. Gamarra *et al.*[15] synthesized CeO_2 nanocubes, nanorods, and nanospheres *via* hydrothermal, microemulsion, and precipitation methods, respectively, and loaded CuO by impregnation. CuO/CeO_2 nanocubes exhibited the highest activity in CO oxidation due to the highly dispersed CuO and the strong interaction between CuO and the (100) faces of CeO_2. Qi *et al.*[10] investigated the effects of cerium precursors, and found that catalysts from the Ce(III) precursor displayed high reducibility and activities in CO oxidation due to the high content of Ce^{3+} and a stronger synergistic effect. Although it was reported that the Cu precursors played an important role in enhancing the dispersion of

[a] *Research Institute of Applied Catalysis, School of Chemical and Environmental Engineering, Shanghai Institute of Technology, Shanghai 201418, PR China. E-mail: dsmao@sit.edu.cn*
[b] *Department of Environmental Science and Engineering, Fudan University, Shanghai 200433, PR China*

active sites in other systems,[11,33–36] to the best of our knowledge, the effect of different Cu precursors on the catalytic activities of CuO/CeO_2 catalysts in CO oxidation has not been investigated in detail so far.

Herein, a series of CuO/CeO_2 catalysts were prepared by impregnating a commercial CeO_2 support with different Cu precursors (acetate, nitrate, chloride, and sulfate), and the effects of Cu precursor and calcination temperature on the nature, dispersion, and redox properties of the obtained Cu species as well as the interaction between Cu species and CeO_2 were systematically investigated. CO oxidation was used as a probe reaction to compare the catalytic activity. The influence of residual anions on the catalytic activity was also studied.

2. Experimental

2.1 Catalyst preparation

All chemicals were of analytical grade from Sinopharm Chemical Reagent Co., Ltd (China) and used without further purification. CuO/CeO_2 catalysts were prepared by impregnating a commercial CeO_2 support (S_{BET} = 11.1 m^2 g^{-1}) with an aqueous solution of $Cu(CH_3COO)_2$, $Cu(NO_3)_2$, $CuCl_2$, or $CuSO_4$ to obtain a Cu loading of 10 wt.%. The CeO_2 support was pre-treated at 120 °C for 4 h before use to remove the impurity adsorbed on the surface. After being impregnated quiescently at room temperature (RT) for 24 h, the sample was dried at 90 °C for 24 h, followed by calcination in static air at 500 or 800 °C for 4 h. For comparison, CuO was prepared by thermal decomposition of $Cu(NO_3)_2$ at 500 °C for 4 h. The prepared catalysts were denoted as CuO/CeO_2(X)-*Y*, where X and *Y* refer to precursor (A for acetate, N for nitrate, C for chloride, and S for sulfate) and calcination temperature (500 or 800 °C), respectively.

2.2 Catalyst characterization

Simultaneous thermogravimetric and differential scanning calorimetric measurements (TG-DSC) were carried out using a NETZSCH STA 449-F3 thermal analyzer made in Germany. The experiments were performed under an air stream of 50 mL min^{-1} from 30 to 1000 °C, at a heating rate of 10 °C min^{-1}.

The actual Cu contents of catalysts after calcination were determined by atomic absorption spectroscopy (AAS) on acid-digested samples, using a SpectrAA-220 atomic absorption spectrometer (VARIAN).

Powder X-ray diffraction (XRD) patterns were recorded on a PANalytical X'Pert instrument using Ni-filtered Cu Kα radiation (λ = 0.15406 nm) at 40 kV and 40 mA. Two theta angles ranged from 10° to 90° with a scanning rate of 6° per minute. The crystallite sizes of CuO and CeO_2 were calculated from the XRD patterns using the Scherrer equation. The lattice parameter values were calculated by the standard cubic indexation method using the intensity of the CeO_2 (111) peak.

N_2 adsorption–desorption isotherms were obtained at −196 °C on a Micrometrics ASAP-2020 adsorption apparatus, after all samples were degassed under vacuum at 300 °C for 10 h. The specific surface areas (S_{BET}) were calculated from the linear part of the Brunauer–Emmett–Teller (BET) plot.

Transmission electron microscopy (TEM) experiments were carried out using a TECNAI microscope operated at 200 kV.

Raman spectra (at 4 cm^{-1} resolution) were obtained with a DXR-Raman instrument (Thermo Fisher Scientific, America) using the 532 nm excitation line (200 mW beam), 5 scans for each spectrum.

The surface compositions and chemical states of the samples were investigated by X-ray photoelectron spectroscopy (XPS, Kratos Axis Ultra DLD spectrometer), using Al Kα radiation. All the binding energy values were calibrated by using C 1s = 284.6 eV as a reference.

H_2 temperature-programmed reduction (H_2-TPR) was carried out in a quartz micro-reactor. Firstly, 20 mg of the as-prepared sample was pretreated at 400 °C in a N_2 stream for 1 h before the TPR measurement. Then the sample was heated to 500 °C at a rate of 5 °C min^{-1} under a flow of H_2 (10 vol%)/N_2 (50 mL min^{-1}). The effluent gas was analyzed by an on-line GC equipped with a TCD.

The CO adsorption properties were measured by temperature-programmed desorption of CO (CO-TPD). The catalyst (0.1 g) was pretreated under He flow (50 mL min^{-1}) with the temperature ramping from 25 to 400 °C at a rate of 10 °C min^{-1}, and then held at 400 °C for 1 h before being cooled down to RT in He flow. The next step was CO adsorption at RT for 0.5 h, and then the gas was swept again with He for 3 h. Subsequently, the sample was heated in flowing He (40 mL min^{-1}) up to 500 °C at a rate of 10 °C min^{-1}, while the desorbed species was detected with a quadrupole mass spectrometer (QMS, Balzers OmniStar 200).

In situ diffuse reflectance infrared Fourier transform spectroscopy (DRIFTS) data were collected using a Nicolet 6700 FT-IR spectrometer fitted with a MCT detector. The DRIFTS cell (Harrick) was fitted with CaF_2 windows and a heating cartridge. The sample in the cell was pretreated in N_2 at 400 °C for 1 h, and then the background was scanned after the cell cooled to 30 °C. After CO (1 vol% CO in Ar) was introduced for 80 min, the IR spectrum of CO adsorbed on the catalyst was recorded. The spectral resolution was 4 cm^{-1} and the number of scans was 64.

2.3 Catalytic activity tests

Prior to the catalytic measurements, the catalyst was pretreated in a N_2 stream (50 mL min^{-1}) at 200 °C for 1 h to remove impurities, and then cooled to RT. The CO oxidation activities of the catalysts were measured in a fixed micro-reactor (6 mm i.d.) under atmospheric pressure with a gas composition of 4 vol% CO, 10 vol% O_2, and 86 vol% N_2 at a space velocity of 9000 mL g^{-1} h^{-1}. A 200 mg catalyst was used for each measurement. The products were analyzed by an

online GC equipped with a flame ionization detector (FID). To allow for the detection of CO and CO_2 with FID, a methanator was inserted between one GC column and the FID.

3. Results and discussion

3.1 Thermal behaviors of the catalyst precursors

The thermal decomposition behaviors of the uncalcined samples dried at 90 °C for 24 h were studied by TG-DSC. As shown in Fig. 1, the course of weight loss is largely dependent on the Cu precursors. The thermal evolution of the CuO/CeO_2(A) precursor in air occurs in three steps. The first step is the dehydration of $CuAc_2{\cdot}H_2O$ into anhydrous copper acetate (from 30 to 135 °C, 0.6% weight loss, eqn (1)). The second step is the decomposition of anhydrous acetate and the formation of Cu_2O (135–280 °C, 11.9% weight loss, close to the theoretical value of 13.5%, eqn (2)). The last step is from 280 to 460 °C with a mass increase of 0.6%, due to the oxidation of Cu_2O to CuO (eqn (3)).[37]

For the CuO/CeO_2(N) precursor, two mass losses can be observed upon heating. The first endothermic peak from 30 to 200 °C with a mass loss of 0.5% is related to the staged dehydration of $Cu(NO_3)_2{\cdot}3H_2O$ into $Cu(NO_3)_2$ accompanied by the thermohydrolysis of $Cu(NO_3)_2{\cdot}2.5H_2O$ to $Cu_2(OH)_3NO_3$ (eqn. (4-1), (4-2) and (5)). The next endothermic peak (200–380 °C) is assigned to the decomposition of $Cu(NO_3)_2$ and $Cu_2(OH)_3NO_3$ into CuO (eqn. (6) and (7)).[38,39] The mass loss (5.8%) is close to the theoretical loss (5.3%) of $Cu_2(OH)_3NO_3$ to CuO, suggesting that a large proportion of Cu species exist as $Cu_2(OH)_3NO_3$ after the CuO/CeO_2(N) precursor is dried at 90 °C for 24 h.

For CuO/CeO_2(A):

$$Cu(CH_3COO)_2 \cdot H_2O \rightarrow Cu(CH_3COO)_2 + H_2O\uparrow \quad (1)$$

$$Cu(CH_3COO)_2 + 3.5O_2 \rightarrow 0.5Cu_2O + 3H_2O\uparrow + 3.5CO_2\uparrow + 0.5CO\uparrow \quad (2)$$

$$Cu_2O + 0.5O_2 \rightarrow 2CuO \quad (3)$$

For CuO/CeO_2(N):

$$Cu(NO_3)_2 \cdot 3H_2O \rightarrow Cu(NO_3)_2 \cdot 2.5H_2O + 0.5H_2O\uparrow \quad (4\text{-}1)$$

$$Cu(NO_3)_2 \cdot 2.5H_2O \rightarrow Cu(NO_3)_2 + 2.5H_2O\uparrow \quad (4\text{-}2)$$

$$Cu(NO_3)_2 \cdot 2.5H_2O \rightarrow 0.5Cu_2(OH)_3NO_3 + H_2O\uparrow + 1.5HNO_3\uparrow \quad (5)$$

$$Cu(NO_3)_2 \rightarrow CuO + 2NO_2\uparrow + 0.5O_2\uparrow \quad (6)$$

$$Cu_2(OH)_3NO_3 \rightarrow 2CuO + HNO_3\uparrow + H_2O\uparrow \quad (7)$$

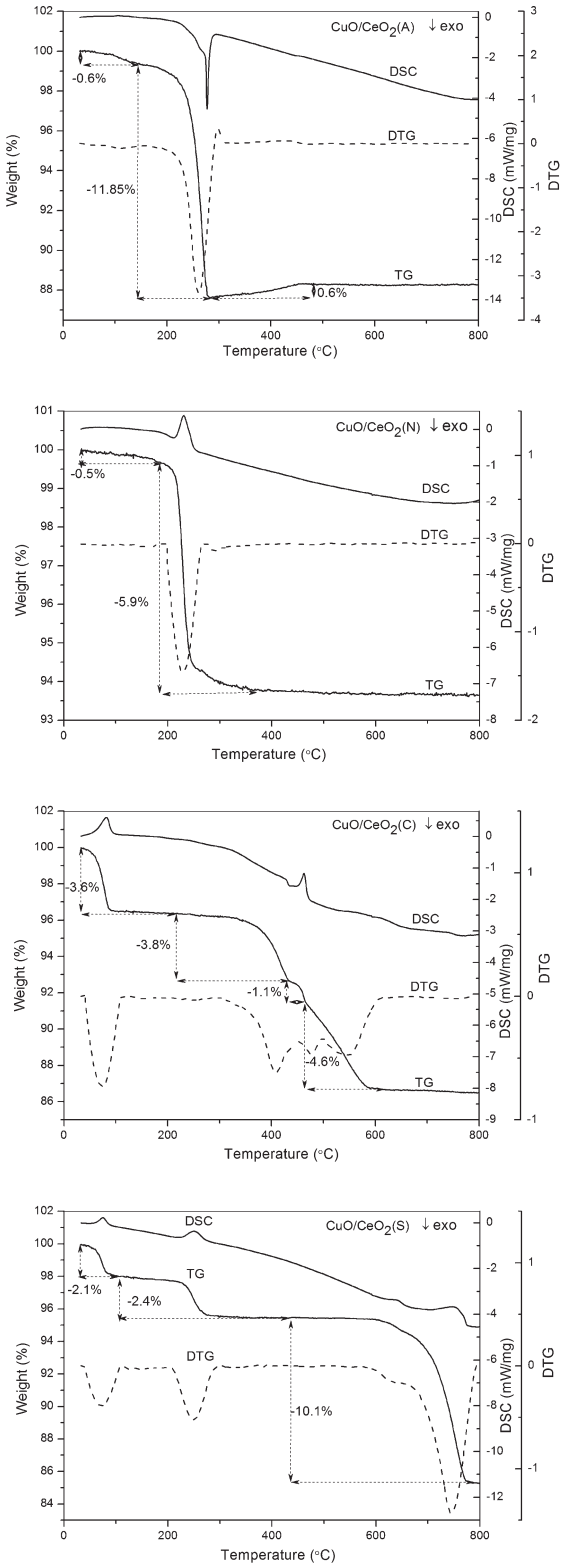

Fig. 1 TG-DSC and DTG (differential thermal gravity, dash line) curves of different CuO/CeO_2 precursors in air (the samples have been dried at 90 °C for 24 h).

The TG data for the CuO/CeO_2(C) precursor in air show four thermal events. Stage I (at about 50–100 °C, 3.5% weight loss) corresponds to the release of coordination water (eqn (8)). Stage II (100–435 °C, 3.8% weight loss) is attributed to the formation of $Cu_2(OH)_3Cl$ from the reaction between $CuCl_2$ and surface oxygen species (eqn (9))[40,41] and the

conversion of $CuCl_2$ into CuCl and Cl_2 (eqn (10)); the produced Cl_2 leaves the sample immediately once formed. Stage III (435–465 °C, 1.1% weight loss), which is absent in the TG curve of pure $CuCl_2{\cdot}2H_2O$, may be due to the partial decomposition of $Cu_2(OH)_3Cl$ into CuO (eqn (11)). The last stage (465–615 °C, 4.6% weight loss) results from the further decomposition of $Cu_2(OH)_3Cl$ and the evaporation of CuCl (eqn (12)).[42,43]

There are three obvious mass losses on the TG curve of the CuO/CeO_2(S) precursor. A mass loss of 2.1% at 50–85 °C is ascribed to the staged dehydration of $CuSO_4{\cdot}5H_2O$ into $CuSO_4{\cdot}H_2O$ (eqn (13-1) and (13-2)); the mass loss is significantly lower than the theoretical loss (10%), due to the loss of water during the drying process. A mass loss (2.5%) at 215–270 °C is assigned to loss of the last water molecule (eqn (14)).[44,45] The last mass loss (10.1%) at 600–780 °C is attributed to the decomposition of $CuSO_4$ into CuO (theoretical loss 10.3%, eqn (15)). Note that the weights of all samples from different precursors do not change further after 800 °C, as shown in Fig. 1.

For CuO/CeO_2(C):

$$CuCl_2 \cdot 2H_2O \rightarrow CuCl_2 + 2\,H_2O\uparrow \quad (8)$$

$$CuCl_2 + 1.5OH^- \rightarrow 0.5Cu_2(OH)_3Cl + 1.5Cl^- \quad (9)$$

$$CuCl_2 \rightarrow CuCl + 0.5Cl_2\uparrow \quad (10)$$

$$Cu_2(OH)_3Cl \rightarrow 2CuO + H_2O\uparrow + HCl\uparrow \quad (11)$$

$$n\mathrm{CuCl} \rightarrow (\mathrm{CuCl})_n\uparrow \quad (12)$$

For CuO/CeO_2(S):

$$CuSO_4 \cdot 5H_2O \rightarrow CuSO_4 \cdot 3H_2O + 2H_2O\uparrow \quad (13\text{-}1)$$

$$CuSO_4 \cdot 3H_2O \rightarrow CuSO_4 \cdot H_2O + 2H_2O\uparrow \quad (13\text{-}2)$$

$$CuSO_4 \cdot H_2O \rightarrow CuSO_4 + H_2O\uparrow \quad (14)$$

$$CuSO_4 \rightarrow CuO + SO_2\uparrow + 0.5O_2\uparrow \quad (15)$$

Therefore, it is clear that different Cu precursors lead to a remarkable diversity in the thermal behaviors of the uncalcined samples, and result in different final products. From the TG-DSC data, we hypothesize that the Cu species on CuO/CeO_2(A)-500, CuO/CeO_2(A)-800, CuO/CeO_2(N)-500, CuO/CeO_2(N)-800, and CuO/CeO_2(S)-800 are just CuO, and the Cu species on CuO/CeO_2(S)-500 is only $CuSO_4$, whereas the nature of Cu species on CuO/CeO_2(C)-500 and CuO/CeO_2-(C)-800 warrants further study.

3.2 XRD and TEM studies

To clarify the Cu species and crystal phases of the catalysts prepared from different precursors before and after calcination (at 500 or 800 °C), the samples were further identified by XRD. The calcination temperatures are determined by thermal analysis data: 500 °C is commonly used for preparing highly active CuO/CeO_2,[7,8] and 800 °C is used to ensure that all samples are in a stable state.

The XRD patterns of different samples prior to calcination are displayed in Fig. 2. All samples exhibit strong diffraction peaks corresponding to CeO_2 (JCPDS 34-0394). In addition, a series of weak diffraction peaks assigned to $Cu(CH_3COO)_2{\cdot}H_2O$ (JCPDS 27-0145), $Cu_2(OH)_3NO_3$ (JCPDS 15-0041), $CuCl_2{\cdot}2H_2O$ (JCPDS 33-0451), and $CuSO_4{\cdot}5H_2O$ (JCPDS 11-0646) can be observed on CuO/CeO_2(A), CuO/CeO_2(N), CuO/CeO_2(C), and CuO/CeO_2(S) precursors, respectively. The presence of $Cu_2(OH)_3NO_3$ on the CuO/CeO_2(N) precursor is consistent with the second weight loss from the TG data (Fig. 1).

Fig. 3 presents the XRD patterns of CuO/CeO_2 obtained by calcining different precursors at 500 or 800 °C. No CeO_2 phase other than cubic CeO_2 can be observed for all of these samples. The characteristic peaks assigned to CuO at 35.5 and 38.7° can be observed for almost all of these samples, except that the Cu species on CuO/CeO_2(S)-500 is actually $CuSO_4$, consistent with the conclusion drawn from the TG analysis.

As shown in Fig. 3a, the characteristic peaks of CuO on CuO/CeO_2(A)-500 and CuO/CeO_2(N)-500 are broad and weak, manifesting that the CuO on these two samples is present as small crystallites and has a disordered structure. Referring to CuO/CeO_2(C)-500, very weak peaks attributed to CuO and $Cu_2(OH)_3Cl$ (JCPDS 50-1559) can be seen, suggesting that most of the Cu species is amorphous or in the form of nanoclusters that cannot be detected by XRD. In addition, the presence of $Cu_2(OH)_3Cl$ and CuO confirms the second and third loss stage on the TG curve of the CuO/CeO_2(C) precursor (Fig. 1).

XRD data for the four samples calcined at 800 °C are shown in Fig. 3b. No other peaks can be observed except for those attributed to CuO and CeO_2. The diffraction peaks of

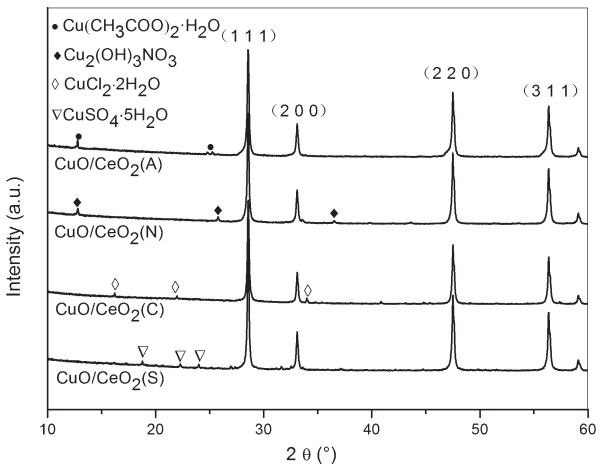

Fig. 2 XRD patterns of the un-calcined samples from different precursors.

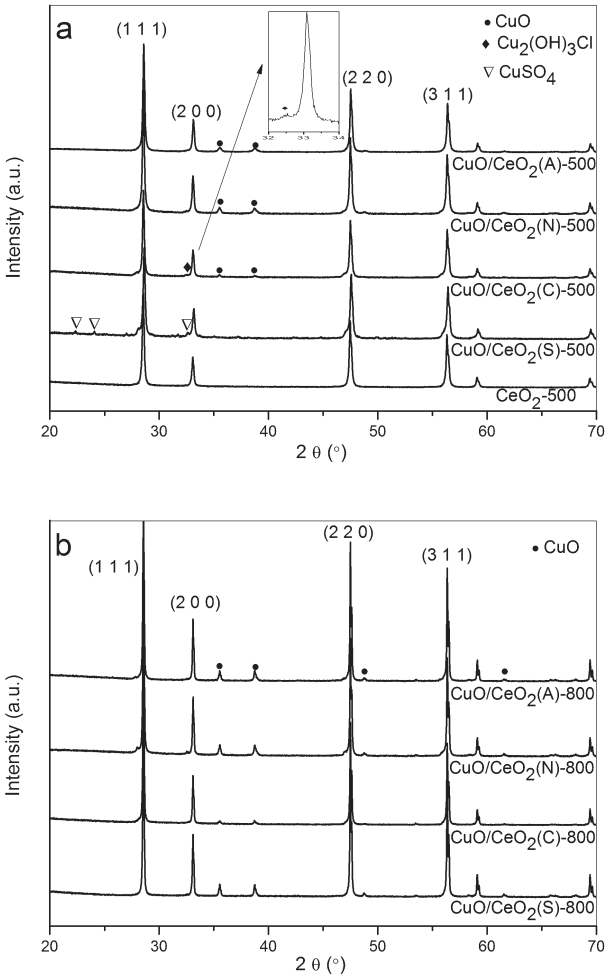

Fig. 3 XRD patterns of the CuO/CeO_2 catalysts calcined at (a) 500 °C and (b) 800 °C.

CuO on CuO/CeO_2(A)-800 and CuO/CeO_2(N)-800 become sharper than their counterparts calcined at 500 °C, indicating the crystallite growth, particle sintering, and ordering of the structure.[16,22] The absence of peaks assigned to $Cu_2(OH)_3Cl$ and $CuSO_4$ on CuO/CeO_2(C)-800 and CuO/CeO_2(S)-800, respectively, may result from the decomposition of $Cu_2(OH)_3Cl$ and $CuSO_4$ into CuO at high temperature. The conversion of $Cu_2(OH)_3Cl$ was also reported by others,[46] while the decomposition of $CuSO_4$ is demonstrated by our TG-DSC data. However, the characteristic peaks assigned to CuO on CuO/CeO_2(C)-800 are still very weak, probably due to the significant loss of Cu content as shown in TG analysis and determined by AAS (Table 1).

Table 1 lists the particle sizes of CuO and CeO_2 on the catalysts estimated by the Scherrer formula. CuO particle size on different catalysts increases approximately in the order of CuO/CeO_2(A)-500 < CuO/CeO_2(C)-500 < CuO/CeO_2(N)-500 < CuO/CeO_2(N)-800 < CuO/CeO_2(C)-800 < CuO/CeO_2(A)-800 < CuO/CeO_2(S)-800. The smallest CuO particles can be obtained on CuO/CeO_2(A)-500. In contrast, the largest CuO particles exist on CuO/CeO_2(S)-800, implying that CuO species derived from the thermal decomposition of $CuSO_4$ sinter easily. CuO/CeO_2(A)-800 has the second largest CuO particles, indicating that CuO from copper acetate is also very unstable as the calcination temperature increases. The TEM images of the CuO/CeO_2(A) calcined at different temperatures are shown in Fig. 4. It is clear that the particles are severely agglomerated with calcination temperature rising from 500 to 800 °C. In addition, the catalyst from copper nitrate has the largest CuO particles at low calcination temperature but a minimal size when the calcination temperature is raised to 800 °C, suggesting that CuO crystals from copper nitrate are more stable than those from other precursors.

The changes in the lattice parameter obtained from the CeO_2 (111) are also shown in Table 1. It is clear that lattice constriction has taken place on all the CuO/CeO_2 catalysts comparing with pure CeO_2, consistent with the results of Martínez-Arias and Luo *et al.*[7,9,24] According to previous research,[7,23] two factors affect the lattice parameter of CeO_2: (1) the substitution of larger Ce^{4+} (0.097 nm) with smaller Cu^{2+} (0.072 nm) contracts the CeO_2 cell; (2) the formation of oxygen vacancies caused by the aliovalent doping (Ce^{4+} by Cu^{2+}) or creation of Ce^{3+} (0.103 nm) sites has an opposite effect. Therefore, it can be inferred that some Cu^{2+} ions have been incorporated into the CeO_2 lattice in our catalysts even though these catalysts were prepared by impregnation.[4,24]

As presented in Table 1, CuO/CeO_2(A)-500 and CuO/CeO_2(S)-500 exhibit more cell constriction of CeO_2 from 0.5414 to 0.5405 and 0.5399 nm, respectively. This may be related to a large amount of highly dispersed CuO or $CuSO_4$ on them,

Table 1 Structural and textural properties of the support CeO_2 and the CuO/CeO_2 catalysts

Catalyst	Cu species	Cu content/mass%	D_{CuO}[a]/nm	D_{CeO_2}[b]/nm	S_{BET}/($m^2\ g^{-1}$)	Lattice parameter[b]/nm
CeO_2-500	—	—	—	37.9	11.05	0.5414
CuO/CeO_2(A)-500	CuO	10.24	24.2	38.8	10.19	0.5405
CuO/CeO_2(N)-500	CuO	10.17	27.7	37.7	8.66	0.5411
CuO/CeO_2(C)-500	CuO, $Cu_2(OH)_3Cl$	9.85	26.0	39.8	8.54	0.5411
CuO/CeO_2(S)-500	$CuSO_4$	10.08	—	33.1	10.62	0.5399
CuO/CeO_2(A)-800	CuO	11.44	41.0	61.0	2.35	0.5411
CuO/CeO_2(N)-800	CuO	10.72	36.6	52.7	4.19	0.5411
CuO/CeO_2(C)-800	CuO	6.88	39.1	58.8	4.27	0.5411
CuO/CeO_2(S)-800	CuO	10.40	47.3	57.5	2.79	0.5412

[a] The particle size of CuO is the average of the calculated values based on CuO (002) and CuO (111). [b] The particle size and lattice parameter of CeO_2 are based on CeO_2 (111) plane.

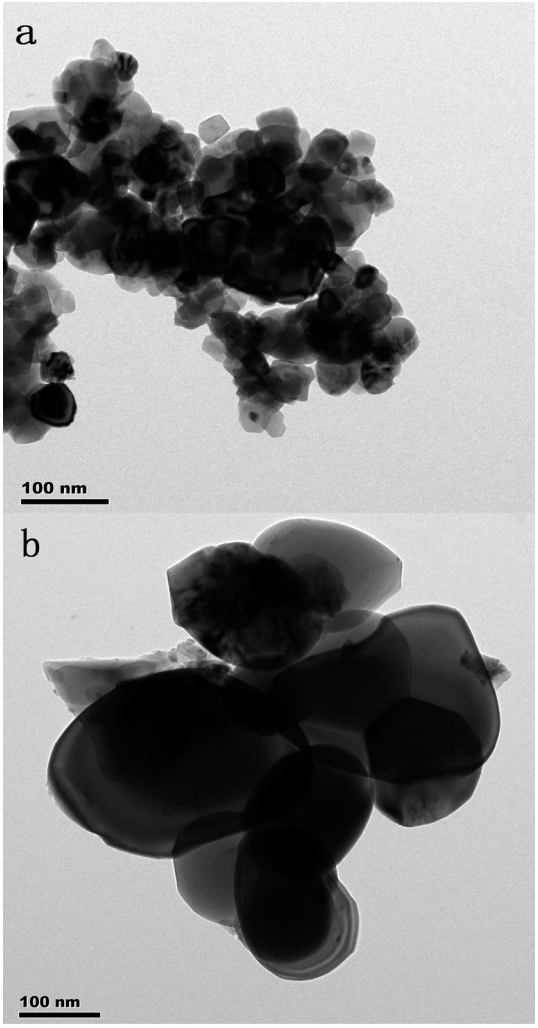

Fig. 4 TEM images of different samples: (a) CuO/CeO_2(A)-500 and (b) CuO/CeO_2(A)-800.

which facilitates the incorporation of Cu^{2+} into the CeO_2 lattice. However, there is no obvious constriction of the CeO_2 cell in CuO/CeO_2(C)-500 with a lot of finely dispersed $Cu_2(OH)_3Cl$ and CuO as well. According to the literature,[47] it can be hypothesized that a certain amount of Cu^{2+} has been introduced into the CeO_2 lattice followed by the formation of cell contraction and oxygen vacancies. However, the produced oxygen vacancies are slightly substituted with the residual Cl^- ions (the ionic radius of Cl^-, 0.181 nm, is significantly larger than that of O^{2-}, 0.135 nm, in the CeO_2 lattice), leading to a lattice expansion. Therefore, CuO/CeO_2(C)-500 shows a slight lattice contraction under the combined effects. However, no CeOCl is observed on XRD patterns, perhaps because the amount of oxygen vacancies and/or Cl^- in our sample is too low to form an adequate quantity of CeOCl that can be detected by XRD. As we know, CuO particles prefer to agglomerate on CeO_2 as the calcination temperature increases, leading to only a small amount of Cu^{2+} incorporated into the lattice, which gives rise to a slight lattice constriction (Table 1).

Therefore, it can be concluded that the Cu precursor and calcination temperature have a significant influence on the final products, including the composition of Cu species, the dispersion capacity of Cu species and the lattice structure of support CeO_2. More specifically, when the samples are calcined at 500 °C, CuO/CeO_2 is obtained from copper acetate, copper nitrate, and copper chloride precursors. Moreover, CuO from copper acetate shows a smaller particle size and better dispersion. In addition, $Cu_2(OH)_3Cl$ can also be obtained from copper chloride besides CuO. $CuSO_4/CeO_2$ is obtained using a copper sulfate precursor. Nevertheless, when the samples are calcined at 800 °C, only CuO/CeO_2 can be obtained from all the Cu precursors.

3.3 BET surface area measurements

The BET surface areas of the CeO_2 support and CuO/CeO_2 catalysts are listed in Table 1. All catalysts exhibit lower specific surface areas than CeO_2 support, probably due to the blocking of the pores of CeO_2 by Cu species.[6] Among them, CuO/CeO_2(S)-500 shows the highest BET surface area, presumably resulting from the highly dispersed $CuSO_4$ and smaller CeO_2 particles as exhibited in our XRD data. CuO/CeO_2(A)-500 with smaller CuO particles has a relatively big surface area as well. When the calcination temperature is raised to 800 °C, the surface areas of all the catalysts decrease significantly as a result of the growth of CeO_2 and CuO crystallites. However, CuO/CeO_2(C)-800 with large CuO and CeO_2 particle sizes shows the highest surface area in all the catalysts calcined at 800 °C, probably due to the lowest CuO content on it.

3.4 Raman analysis

Raman analysis is a potential tool to obtain additional structural information, because it is sensitive to crystalline symmetry and oxygen lattice vibrations[48] in contrast to the XRD results.

Fig. 5 shows the Raman spectra of CeO_2 and different catalysts. In Fig. 5a, a strong peak at 460 cm^{-1}, corresponding to the F_{2g} Raman vibration mode of fluorite CeO_2,[14,15,24,49] can be observed on all samples. Once the Cu species is introduced, two new peaks at about 235 cm^{-1} and 600 cm^{-1} appear on the CuO/CeO_2 catalysts. The weak band at 235 cm^{-1} is attributed to the displacement of oxygen atoms from their ideal fluorite lattice positions.[14] The broad band at 600 cm^{-1} is often related to the presence of oxygen vacancies in the CeO_2 lattice.[15,24,49] In addition, the presence of a weak peak at 300 cm^{-1} on CuO/CeO_2(N)-500 is compatible with the presence of larger CuO particles as shown in XRD data. The appearance of oxygen vacancies on all catalysts indicates the incorporation of Cu^{2+} into the CeO_2 lattice, in agreement with the microstrain values observed for them as shown in Table 1. The relatively higher intensity of the band at 600 cm^{-1} can be obtained for CuO/CeO_2(C)-500 and CuO/CeO_2(S)-500, indicating that more oxygen vacancies have been formed. In addition, the high concentration of oxygen

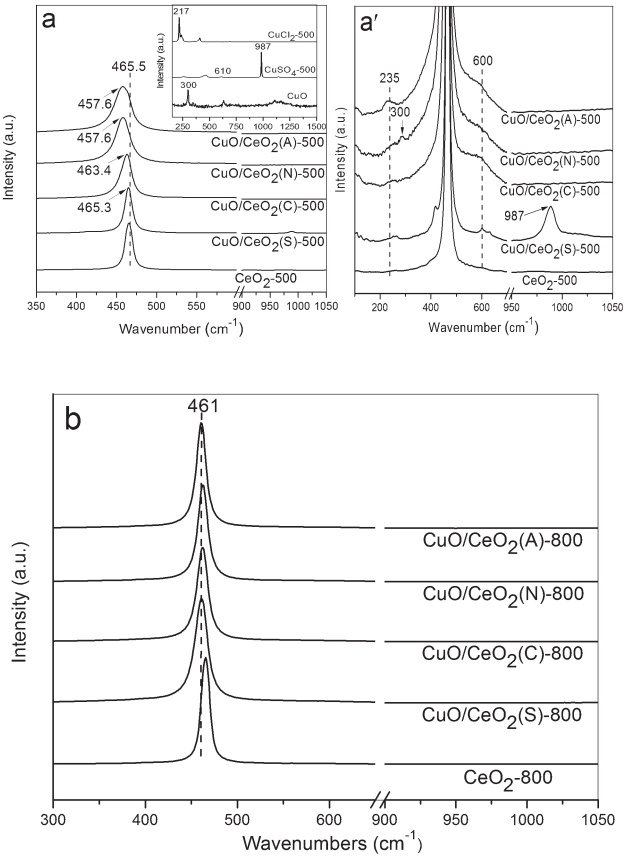

Fig. 5 Raman spectra of different CuO/CeO_2 catalysts calcined at (a) 500 °C (a′ is the enlarged view of (a)) and (b) 800 °C.

vacancies on CuO/CeO_2(C)-500 further supports the surmise of the formation of CeOCl, as mentioned in XRD analysis. Meanwhile, a small peak at 1000 cm^{-1} assigned to $CuSO_4$ (inset in Fig. 5a) can also be observed on CuO/CeO_2(S)-500, in agreement with the XRD results (Fig. 3a and Table 1).

On the other hand, a small redshift and broadening of the F_{2g} band are observed on all the catalysts compared with pure CeO_2 (465.5 cm^{-1}). This phenomenon may be due to the incorporation of Cu in the CeO_2 lattice (which induces the distortion of the lattice).[14,28,49,50] However, the redshift and broadening of the F_{2g} band, ranked in the order of CuO/CeO_2(S)-500 < CuO/CeO_2(C)-500 < CuO/CeO_2(N)-500 < CuO/CeO_2(A)-500, change nonlinearly with the variation of the lattice parameter and the amount of oxygen vacancies. Especially, F_{2g} bands of CuO/CeO_2(S)-500 (465.3 cm^{-1}) and CuO/CeO_2(C)-500 (463.4 cm^{-1}) with more oxygen vacancies and residual anions show a smaller redshift and broadening than the F_{2g} bands of CuO/CeO_2(A)-500 (457.6 cm^{-1}) and CuO/CeO_2(N)-500 (457.6 cm^{-1}) with only CuO particles. This result indicates that different Cu species and CuO–CeO_2 interaction may have an influence on the lattice structure of CeO_2 as well. In fact, an earlier work[7] suggested that the Cu species interacting with CeO_2 can also impact the micro-strain values, thus influencing the position and full width at half-maximum (FWHM) values of the F_{2g} band. Thus, from the results mentioned above it can be inferred that interaction between Cu species and CeO_2 can also affect the lattice structure of CeO_2 and exerts a more important effect on the main F_{2g} mode band than the incorporation of Cu into the CeO_2 lattice.

Fig. 5b presents the Raman spectra of the catalysts calcined at 800 °C. The bands at 235 and 600 cm^{-1} almost disappear for all catalysts due to the sintering and growth of CuO and CeO_2 particles (which decrease the amount of Cu^{2+} introduced into the CeO_2 lattice, thus leading to the reduction of oxygen vacancies). On the other hand, a small redshift and broadening of the F_{2g} band are also observed for all catalysts compared with CeO_2 calcined at 800 °C, suggesting the presence of residual oxygen vacancies and interaction between CuO and CeO_2. However, the peak position (at about 461 cm^{-1}) and FWHM of the F_{2g} band for different catalysts show similar values, attributed to similar CuO species and metal–support interactions on them (Table 1). Noticeably, the F_{2g} bands of CuO/CeO_2(A)-800 and CuO/CeO_2(N)-800 shift to high wavenumbers, whereas those of CuO/CeO_2(C)-800 and CuO/CeO_2(S)-800 are redshifted compared to the ones prepared by calcining the same precursors at 500 °C. The blue shift is caused by the better crystallization and larger particle sizes of CuO and CeO_2 (ref. 51) formed at a higher calcination temperature, and the redshift may be due to the conversion of isolated Cu^{2+} to CuO and the disappearance of residual anions. This phenomenon further demonstrates that the interaction between Cu species and CeO_2, varying with different Cu species and the residual anions, has an important influence on the micro-strain values of CeO_2.

Therefore, it is clear that different Cu precursors give rise to various Cu species, resulting in different structures and oxygen vacancies of the CeO_2 support. The disparity of Cu species has a predominant influence on the formation of oxygen vacancies, which indicates the amounts of Cu^{2+} doping into the CeO_2 lattice. On the other hand, the metal–support interaction, which may be affected by the residual anions, can affect the lattice structure as well. The strength of metal–support interaction may increase in the order CuO/CeO_2(S)-500 < CuO/CeO_2(C)-500 < CuO/CeO_2(N)-500 < CuO/CeO_2(A)-500, as reflected in the broadening and shift of the F_{2g} band for CeO_2.

3.5 X-ray photoelectron spectroscopy

To further investigate the surface compositions and chemical states of the catalysts, XPS experiments were carried out. Table 2 displays the surface atomic compositions of different catalysts. CuO/CeO_2(N)-500 has more Cu species dispersed on CeO_2 than the catalyst from copper acetate, demonstrated by a higher Cu/Ce atomic ratio and stronger intensity of the Cu 2p peak,[6] whereas CuO/CeO_2(A)-500 has more CeO_2 species, as verified by higher intensity of the Ce 3d peak (Fig. 6c). In addition, it can be seen from the XPS spectra of different catalysts (Fig. 6a) that residual Cl^- and SO_4^{2-} are present on CuO/CeO_2(C)-500 and CuO/CeO_2(S)-500, respectively.

Table 2 XPS data measured for CuO/CeO_2 catalysts from different Cu precursors

Catalyst	Atomic ratio		Ce(III) %	O_{last} %[a]	I_{sat}/I_{pp}[b]	Cu(I) %[c]
	Cu/Ce	Ce/O				
CuO/CeO_2(A)-500	0.5835	0.3778	15.6	6.1	0.54	51
CuO/CeO_2(N)-500	0.7296	0.3077	15.0	1.7	0.56	50
CuO/CeO_2(C)-500	0.3706	0.3549	16.1	7.5	0.61	48
CuO/CeO_2(S)-500	0.1988	0.2708	17.2	15.3	0.66	0

[a] The relative intensity of the third component to total O 1s peak. [b] The ratio of the intensities of Cu 2p satellite peaks to those of the principal peaks. [c] The ratio of Cu^+ peak area to the total area in Cu LMM.

The O 1s, Ce 3d and Cu 2p XPS spectra are shown in Fig. 6(b–d). There are three components on the O1s spectra of different catalysts (Fig. 6b): the main component at about 529 eV is assigned to the lattice oxygen of metal oxides,[18,52] another one at about 531 eV is typical of absorbed oxygen or hydroxide,[52] and the last one at 533.4 eV is assigned to the organic oxygen or the presence of Ce^{3+} surface defects.[18,53] The lowest intensity of the main component on CuO/CeO_2(S)-500 further demonstrates the absence of CuO. The relative intensity of the third component to the total O 1s peak (denominated as O_{last} %) is listed in Table 2. The O_{last} % increases in the order of CuO/CeO_2(N)-500 < CuO/CeO_2(A)-500 < CuO/CeO_2(C)-500 < CuO/CeO_2(S)-500. The relatively higher O_{last} % suggests the presence of more Ce^{3+} surface defects that are accompanied by the formation of oxygen vacancies, in good agreement with the XRD and Raman data.

The Ce 3d XPS data obtained from different catalysts calcined at 500 °C are shown in Fig. 6c. Two sets of spin–orbital multiplets related to $3d_{3/2}$ and $3d_{5/2}$ are labelled as *u* and *v*, respectively. According to previous research,[10,54] the complex spectrum of Ce 3d is decomposed into ten components. Lines v_0 and v' are contributed to the Ce $3d^9$ $4f^2$ O^2 p^5 and the Ce $3d^9$ $4f^1$ O^2 p^6 of Ce(III), respectively; and the same assignment can also be applied to the *u* structures. However, u_0 and v_0 are invisible in our samples, as also reported by Li *et al.*[14] Thus, an acceptable way to calculate the reduction degree of CeO_2 is to consider the relative intensities of the u' and v' peaks to the total Ce 3d region.

$$\mathrm{Ce(III)}\,(\%) = \frac{100\left[S(u') + S(v')\right]}{\Sigma\left[(u) + (v)\right]}$$

The calculated percentages of Ce(III) for different catalysts are listed in Table 2. It can be seen that the reduction of CeO_2 exists on all samples, and the Ce(III) % values increase in the order of CuO/CeO_2(N)-500 < CuO/CeO_2(A)-500 < CuO/CeO_2(C)-500 < CuO/CeO_2(S)-500, consistent with the Ce^{3+} surface defects reflected in the O1s spectra. According to Qi *et al.*,[10] the presence of Ce^{3+} can facilitate the electron transfer process of $Ce^{3+} + Cu^{2+} \leftrightarrow Ce^{4+} + Cu^+$ beneficial for achieving high activities in CO oxidation. Additionally, the values of Ce(III) % for these catalysts are about two times higher than that of pure CeO_2 reported previously (Ce(III) = 6.75%),[55] but the lattice parameters of these samples are similar to the reported one. This may be due to the fact that the sampling depth of XPS is below 10 nm, while the XRD analysis, from which the lattice parameters are determined, is a "bulk" technique. Therefore, large differences exist between the two kinds of analytical tools. In fact, almost all of CeO_2 in the bulk phase are still fully oxidized, thus, the reduction level of CeO_2 observed from XPS has a negligible influence on the lattice parameters. On the contrary, these catalysts show slightly lower lattice parameters caused by the incorporation of Cu^{2+} into the CeO_2 lattice. A similar result was also obtained by Li *et al.*[14]

Comparing the XPS spectra of Cu 2p for different samples, the Cu^{2+} component (showing the principal peaks at 934.3 eV and the satellite peaks at 938–948 eV) is observed on all catalysts. Moreover, the Cu^+ or Cu^0 component (at 932.4 eV) can also be found for the catalysts except for CuO/CeO_2(S)-500. The reduced degree of Cu species can be investigated by calculating the ratio of the intensities of the satellite peaks to those of the principal peaks (I_{sat}/I_{pp}, shown in Table 2). The value of I_{sat}/I_{pp} is 0.66 in CuO/CeO_2(S)-500, on which all of the Cu species are in the divalent oxidation state. This value is lower on the other catalysts. Therefore, a slightly reduced Cu phase is present on CuO/CeO_2(A)-500, CuO/CeO_2(N)-500, and CuO/CeO_2(C)-500. This phenomenon indicates that the strong interaction between CuO and CeO_2 has induced the slight reduction of surface Cu^{2+} into Cu^+ (ref. 1, 10 and 52) regarded as the better CO adsorption site in CO oxidation,[10,24] even at room temperature. The absence of Cu^+ on CuO/CeO_2(S)-500 may be due to the synergistic effects interdicted by the presence of SO_4^{2-}. It is well known that the Cu_{2p} XPS peaks cannot be used to distinguish between Cu^+ and Cu^0, because they are essentially identical. However, the Cu LMM Auger lines of Cu^+ and Cu^0 are separated by about 2.0 eV, allowing easy distinction between the two species. It is clear in Fig. 6e that the reduced Cu species mainly exist as Cu^+ (916.3 eV),[10] except for CuO/CeO_2(S)-500, on which the relatively lower kinetic energy of Cu LMM Auger lines may be related to the presence of SO_4^{2-}. The ratios of the Cu^+ area to the total area (denoted as Cu(I) %), shown in Table 2, for CuO/CeO_2(A)-500, CuO/CeO_2(N)-500 and CuO/CeO_2(C)-500 are almost the same, suggesting that the Cu^+ contents on them are similar. Note that the Cu(I) % is just calculated for comparison and does not represent the accurate content

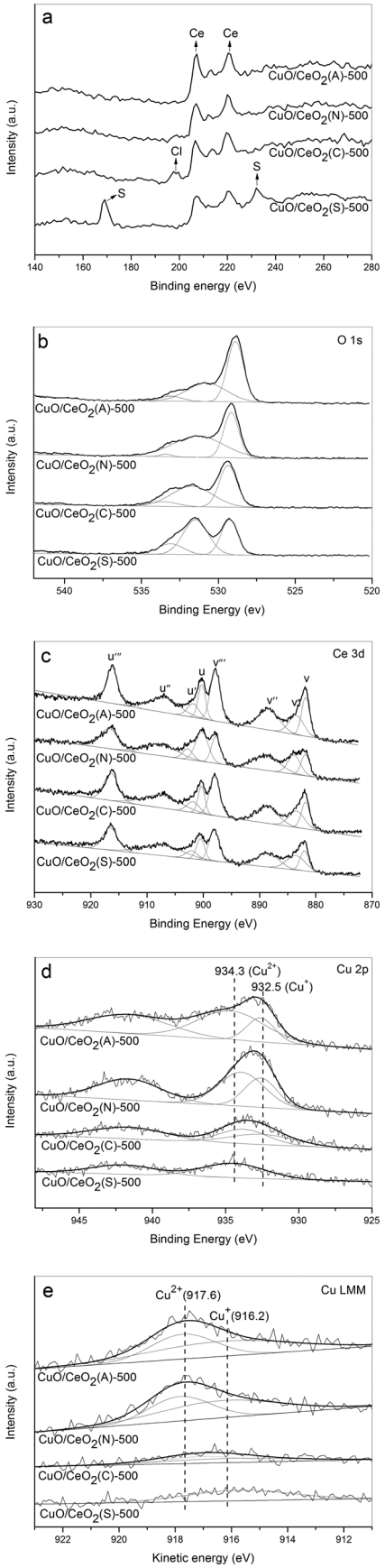

Fig. 6 XPS spectra of different CuO/CeO_2 catalysts: (a) wide, (b) O1s, (c) Ce3d, (d) Cu2p and (e) Cu LMM.

of Cu^+ on CuO/CeO_2 catalysts due to the lower Cu content and the photoresolution in the spectrometer.

By comparing the XPS results of catalysts from different Cu precursors, it can be observed that Cu precursors influence the Ce^{3+} content of surface CeO_2, which is associated with the formation of oxygen vacancies. Additionally, strong synergistic effects between CuO and CeO_2 can induce the reduction of Cu^{2+} to Cu^+ which is regarded as a more active CO adsorption site. However, the presence of residual SO_4^{2-} inhibits the synergistic effects, resulting in the absence of Cu^+ on CuO/CeO_2(S)-500.

3.6 H_2-TPR characterization

H_2-TPR experiments were conducted to investigate the reduction properties of CuO/CeO_2. CuO obtained by thermal decomposition of copper nitrate at 500 °C for 4 h shows a single reduction peak at around 255 °C, attributed to the complete reduction of Cu^{2+} to Cu^0 (inset in Fig. 7a). CeO_2 has two reduction peaks at about 550 and 900 °C, ascribed to the reduction of surface and bulk oxygen species, respectively.[56]

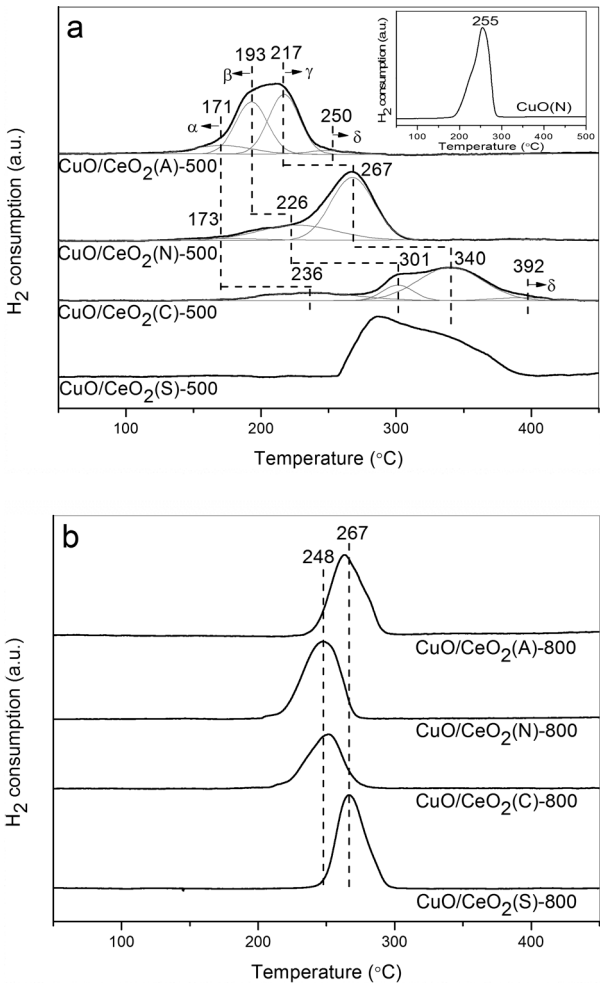

Fig. 7 H_2-TPR profiles of CuO/CeO_2 catalysts calcined at 500 °C (a) and 800 °C (b).

The H_2-TPR curves of CuO/CeO_2 catalysts calcined at 500 °C are shown in Fig. 7a. Except for CuO/CeO_2(S)-500, three reduction peaks corresponding to three different types of Cu species entities differing in their degree of interaction with the support can be found on the other catalysts.[2,14] Peak α at low temperature is ascribed to the reduction of finely dispersed Cu species strongly interacting with CeO_2; peak β at higher temperature is assigned to the reduction of larger particles of Cu species; peak γ is attributed to the reduction of bulk Cu species interacting weakly with CeO_2.[15,24] The reducible Cu species on CuO/CeO_2(A)-500 and CuO/CeO_2(N)-500 are CuO only, while the reduction of $Cu_2(OH)_3Cl$ species also contributes to the reduction peaks for CuO/CeO_2(C)-500.[57,58] In addition, for CuO/CeO_2(A)-500 and CuO/CeO_2(C)-500, high temperature peaks at 250 and 392 °C (peak δ), respectively, are required for satisfactory fitting of the profile. This may correspond to the reduction of Cu^{2+} in the CeO_2 lattice, which is proposed to be the most difficult to reduce.[9,15] There are also a series of peaks on the TPR profile of CuO/CeO_2(S)-500, maybe due to the complex reactions between $CuSO_4$ and H_2, which are not studied in detail in this paper.

Specifically, it can be seen from the profiles of CuO/CeO_2-(A)-500 that all of these reduction temperatures are lower than that of pure CuO, indicating that the presence of CeO_2 facilitates the reduction of CuO. On the other hand, by integrating the area of the reduction peak, the H_2 uptake is calculated. The actual H_2 consumption of CuO/CeO_2 catalysts, except for CuO/CeO_2(S)-500, during the TPR test up to 450 °C is higher than that required for full reduction of Cu species, indicating that the reduction of surface CeO_2 must also contribute to the observed reduction peaks. The synergistic effect between CuO and CeO_2 is believed to enhance their individual reducibility.[10,56] The lower reduction temperature of CuO and a large amount of excess H_2 uptake (219 μmol g^{-1}) obtained on CuO/CeO_2(A)-500 suggest stronger synergistic effects and more reducible surface CeO_2 on it.

A quantitative attribution of the TPR peaks to different species has been calculated and the results are shown in Table 3. It is clear that CuO/CeO_2(C)-500 has more finely dispersed Cu species (21%) than CuO/CeO_2(A)-500 and CuO/CeO_2(N)-500, consistent with the results obtained from XRD. However, the reduction temperature of Cu species on CuO/CeO_2(C)-500 shifts to a higher temperature than that on CuO/CeO_2(A)-500 and CuO/CeO_2(N)-500. Especially, the reduction temperature of bulk CuO on it (340 °C) is even significantly higher than that of pure CuO particles (255 °C); this may be caused by the presence of Cl^-, which inhibits the reduction of Cu species. Additionally, the excess H_2 uptake (56 μmol g^{-1}) of CuO/CeO_2(C)-500 is relatively lower. Thus, it can be inferred that the presence of Cl^- has a negative influence on the synergistic effects between Cu species and CeO_2, leading to a poor reducibility of surface CeO_2 species. According to Fajardie and Abid *et al.*,[47,59] the presence of Cl^- could give rise to CeOCl located at the interface between CeO_2 and CuO. The CeOCl phase will change the interaction between CuO and CeO_2 and present a barrier to the hydrogen spillover from highly dispersed CuO to CeO_2,[47,59] thus leading to an inhibiting effect on the reduction of the CeO_2 surface. On the other hand, CuO/CeO_2(A)-500 and CuO/CeO_2(C)-500 also show some Cu^{2+} species in the CeO_2 lattice (4% and 5%, respectively), in agreement with the XRD and Raman analyses. The absence of Cu^{2+} incorporated into the CeO_2 lattice on CuO/CeO_2(N)-500 suggests that almost all the CuO exist on the CeO_2 surface, leading to a higher Cu/Ce atomic ratio as shown in XPS data (Table 2).

It can be seen from Fig. 7b that only one reduction peak at around 260 °C, corresponding to the reduction of bulk CuO, can be observed on all CuO/CeO_2 catalysts calcined at 800 °C; and a similar peak position and shape may be related to the same CuO phase and similar particle size on them as reflected in XRD results (Table 1). In the case of CuO/CeO_2-(A)-800, the reduction of bulk CuO shifts to a higher temperature than that of the counterpart prepared by calcination at 500 °C, due to the sintering and growth of CuO and CeO_2 particles as the temperature increases.[16,22] Almost no change happens on the reduction temperature of bulk CuO on CuO/CeO_2(N) samples with different calcination temperatures, suggesting that the bulk CuO from copper nitrate is more stable. Furthermore, the reduction of bulk CuO on CuO/CeO_2(C)-800 shifts towards a lower temperature than that on CuO/CeO_2(C)-500, probably due to the disappearance of the inhibiting effects caused by Cl^-. Most of Cl^- ions may have been eliminated when the catalyst is calcined in air at 800 °C for 4 h.[47] As for the two CuO/CeO_2(S) catalysts

Table 3 Results of H_2-TPR analysis

Sample	Reduction temperature (°C) and relative intensities[a] (%)				Total H_2 consumption (μmol g^{-1})	Excess H_2 consumption (μmol g^{-1})
	α	β	γ	δ		
CuO/CeO_2(A)-500	171 (12)	193 (39)	217 (45)	250 (4)	1444	194
CuO/CeO_2(N)-500	173 (4)	226 (30)	267 (66)	—	1382	132
CuO/CeO_2(C)-500	236 (21)	301 (14)	340 (60)	392 (5)	1219	56
CuO/CeO_2(S)-500	—	—	—	—	—	—
CuO/CeO_2(A)-800	—	—	263	—	1257	7
CuO/CeO_2(N)-800	—	—	248	—	1344	94
CuO/CeO_2(C)-800	—	—	252	—	933	73
CuO/CeO_2(S)-800	—	—	267	—	1290	40

[a] Peak area in percentage of total area.

prepared at different temperatures, the distinction may come from the different reducible properties of CuO and $CuSO_4$.

CuO/CeO_2(C)-800 displays a minimum H_2 consumption, resulting from the volatilization of CuCl during the calcination process as shown in TG analysis. Moreover, the excess H_2 consumptions of CuO/CeO_2(A) and CuO/CeO_2(N) decrease obviously as the calcination temperature increases, attributable to the decrease in active surface CeO_2. According to the literature,[16] the agglomeration and growth of CuO and CeO_2 particles will weaken the CuO–CeO_2 interaction, leading to a poor reducibility of surface CeO_2. The abnormality that happened on CuO/CeO_2(C) and CuO/CeO_2(S) may be related to the residual anions. The results mentioned above indicate that the strong synergistic effect can promote the reducibility of Cu species and surface CeO_2, and the effect is significantly affected by residual anions and the calcination temperature.

3.7 CO-TPD study

Typical TPD profiles of CO_2 after CO adsorption at 30 °C for 30 min on different catalysts are given in Fig. 8. Almost all the adsorbed CO has been released after the sample is purged under flowing He at room temperature. In the heating process, the majority of adsorbed CO desorbs as CO_2 resulting from different carbonate species produced by the reaction of absorbed CO with lattice oxygen,[2,60] and only a small quantity of CO desorbs from CuO/CeO_2(C)-500 at low temperatures with a peak at 58 °C as shown in Fig. 9. It can be seen from Fig. 8(a) that there are two CO_2 desorption peaks on CuO/CeO_2(A)-500 and CuO/CeO_2(N)-500, including a main peak at around 130 °C and a shoulder peak at about 287 °C, consistent with the results of Avgouropoulos and Ioannides.[61] According to the literature,[60] the peaks may be related to the different CO adsorption approach: a fraction of CO has formed CO_2 at room temperature, which probably reacts with the CeO_2 surface and adsorbed as carbonate, and releases at about 100 °C; another fraction of the CO probably develops into bidentate carbonate on the reactive sites, which may evolve across intermediate species (maybe as CO_x) when the temperature increases and finally desorbs as CO_2 at higher temperatures (200–400 °C).

The CO-TPD profile of CuO/CeO_2(A)-500 shows the highest intensity and the lowest temperature for CO_2 desorption at 129 °C, implying that there are more active lattice oxygen that can interact with the adsorbed CO to form CO_2 at room temperature and the produced carbonate species can desorb easily, beneficial for enhancing the catalytic activity.[2,62,63] The enhanced activity of lattice oxygen may be resulted from more finely dispersed CuO and the stronger CuO–CeO_2 synergistic effect. In contrast, drastic differences can be found on CuO/CeO_2(C)-500, CuO/CeO_2(S)-500, and CeO_2-500. As shown in Fig. 8a, only one CO_2 desorption peak at around 270 °C can be seen on CuO/CeO_2(C)-500; this peak may be related to the second CO adsorption approach as discussed above and suggests that almost no CO_2 formed at room temperature (the first CO adsorption approach). For CuO/CeO_2(S)-500 and

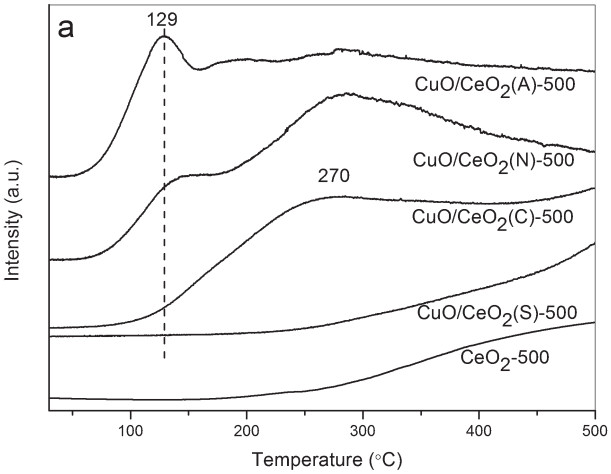

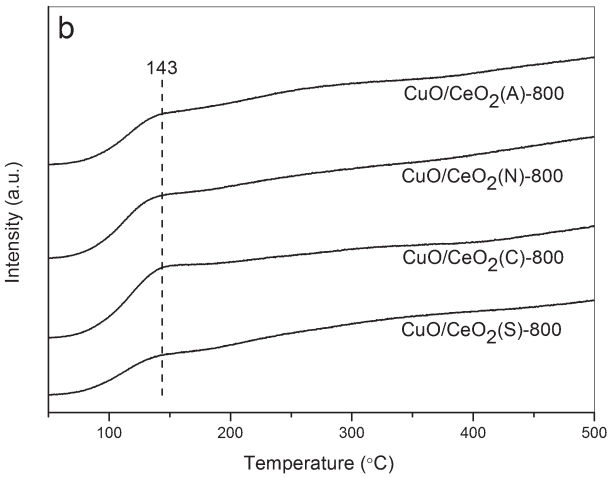

Fig. 8 TPD profiles of CO_2 after CO adsorption at ambient temperature for 30 min over CuO/CeO_2 catalysts calcined at 500 °C (a) and 800 °C (b).

CeO_2-500, no peaks but a slight increase in CO_2 signal is observed, indicating that only a small amount of bidentate

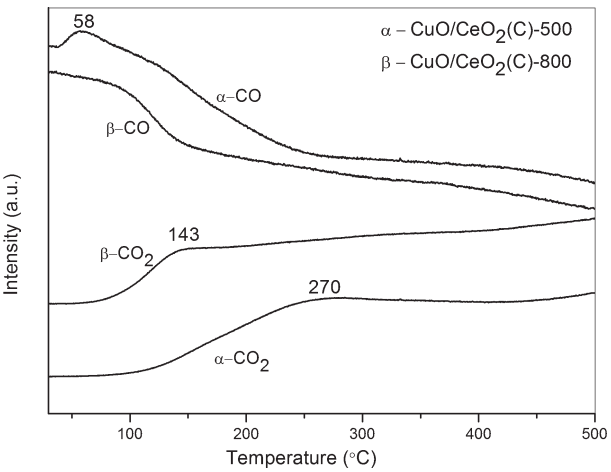

Fig. 9 CO and CO_2 TPD profiles for CuO/CeO_2(C) catalysts after adsorbing CO at ambient temperature for 30 min.

carbonate species formed on them.[61] Importantly, CuO/CeO_2-(S)-500 even exhibits a smaller CO_2 desorption than pure CeO_2 due to the absence of CO adsorption sites and the partial coverage and poison of the CeO_2 surface by SO_4^{2-}.

Fig. 8(b) presents the CO-TPD profiles of CuO/CeO_2 catalysts calcined at 800 °C. All samples exhibit a CO_2 desorption peak at about 143 °C as a result of similar CuO and CeO_2 species on them. CuO and CeO_2 particles can sinter and enlarge as the temperature increases, leading to a decrease in the dispersion of CuO and a weakening of the synergistic effects. Thus, comparing with the counterparts calcined at 500 °C, the intensity of CO_2 desorption peaks for the catalysts calcined at 800 °C decreases considerably, as a result of the reduction of active lattice oxygen that can react with CO at room temperature, except for the catalyst obtained from the copper sulfate precursor. The diversity observed with CuO/CeO_2(S) is mainly due to the different profiles of CuO and $CuSO_4$ and the inhibiting effect of SO_4^{2-} on the synergistic effects. In addition, the low temperature CO_2 desorption peak on CuO/CeO_2(A)-800 shifts to a higher temperature than that on CuO/CeO_2(A)-500 as a result of the sintering of CuO, whereas no obvious shift can be observed for CuO/CeO_2(N), suggesting that CuO particles from copper acetate are less stable than those from copper nitrate as the calcination temperature increases.

The CO and CO_2 signals derived simultaneously from CO-TPD of CuO/CeO_2(C) calcined at different temperatures are shown in Fig. 9. Notably, a very weak peak for CO desorption is visible at 58 °C on CuO/CeO_2(C)-500, while it is absent on other catalysts (not shown here); this peak may be related to the desorption of CO adsorbed on the finely dispersed Cu species. The adsorbed CO can be removed easily, but cannot be oxidized by lattice oxygen at room temperature. This phenomenon further confirms the speculation that the presence of Cl^- decreases the activity of lattice oxygen species. When the calcination temperature rises to 800 °C, highly dispersed Cu species have almost disappeared, leading to the absence of the corresponding CO desorption peak. What is more, most of Cl^- ions have been eliminated, thus, the inhibiting effect on the CuO–CeO_2 interaction has disappeared and lattice oxygen becomes more active under the synergistic effects. As a result, a fraction of adsorbed CO can react with lattice oxygen to form CO_2 at lower temperature, and the low temperature CO_2 desorption peak (the first CO adsorption approach) appears on CuO/CeO_2(C)-800 in contrast to CuO/CeO_2(C)-500.

Thus, it can be concluded that different Cu precursors and calcination temperatures affect the CO adsorption approach and the activity of lattice oxygen, which is regarded as more active than gas-phase oxygen,[5,10,28] and may lead to different CO oxidation abilities.

3.8 *In situ* DRIFTS study

In situ DRIFTS experiments of CO as a probe molecule were conducted to further investigate the influence of Cu precursors on the CO adsorption properties of the CuO/CeO_2 catalysts. As shown in Fig. 10, CuO/CeO_2(A)-500, CuO/CeO_2-(N)-500, and CuO/CeO_2(C)-500 show a strong peak at about 2108–2125 cm^{-1} assigned to the linear CO adsorbed on Cu^+ sites (Cu^+–CO),[10,14,24,64,65] in agreement with the Cu(I) % calculated from XPS spectra. Nevertheless, this peak is invisible on CeO_2 and negligible on CuO/CeO_2(S)-500 and CuO. Thus, the inhibition of the synergistic effect by SO_4^{2-} has led to the lower CO adsorption properties for CuO/CeO_2(S)-500. Additionally, considering that the Cu^+–CO species detected on pure Cu_2O gives a main IR adsorption band at about 2127 cm^{-1} (ref. 66) and the interaction between copper and CeO_2 can make the band shift to lower wavenumbers according to previous contributions,[14,65] it can be concluded that the strengths of synergistic effects, based on the peak position of the Cu^+–CO band, follow the sequence of CuO/CeO_2(C)-500 < CuO/CeO_2(N)-500 < CuO/CeO_2(A)-500. The relatively higher wavenumber of the IR adsorption band for Cu^+–CO species and weaker synergistic effects on CuO/CeO_2(C)-500 may result from the presence of Cl^- at the CuO–CeO_2 interface.

The spectral zone below 1600 cm^{-1} presents several peaks ascribed to carbonate or formate species chemisorbed on CeO_2. The peak at about 1470 cm^{-1} is attributed to the antisymmetric stretching of the terminal CO bonds in poly- or mono-dentate carbonates;[65,67] the peaks at 1385 and 1318 cm^{-1} are ascribed to formate[10,65] and bidentate carbonates associated with CeO_2,[17,21] respectively. The generation of carbonate or formate species can be found obviously on CuO/CeO_2(A)-500, CuO/CeO_2(N)-500, and CeO_2. The formation of carbonate is basically related to the reaction between lattice oxygen on the CeO_2 surface and CO_2 formed by CO oxidation.[17] Thus, the relatively higher intensity of carbonate on CuO/CeO_2(A)-500 indicates that plentiful CO_2 have been formed by the reaction between CO and CuO or CeO_2 and

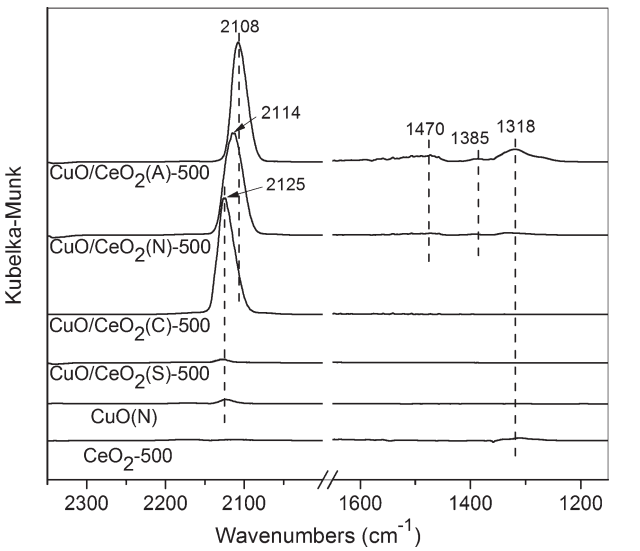

Fig. 10 DRIFTS spectra recorded after introducing CO for different CuO/CeO_2 catalysts calcined at 500 °C (the spectra were recorded at 30 °C after introducing 1 vol% CO in He mixture).

the lattice oxygen on the CeO_2 surface is more active caused by the stronger synergistic effects, while the absence of carbonate on CuO/CeO_2(S)-500 suggests that no CO_2 is produced and the CeO_2 surface (partly covered by SO_4^{2-}) is less active. On the other hand, carbonate species are also invisible on CuO/CeO_2(C)-500; this may be due to the presence of Cl^- that lowers the activity of lattice oxygen on the CeO_2 surface (thus inhibiting the formation of these species).

Therefore, it can be concluded that Cu^+ formed under the synergistic effects is the better CO adsorption site than Cu^{2+}. Moreover, the CO adsorption properties and activity of lattice oxygen on the CeO_2 surface for different catalysts are seriously affected by the Cu precursors and ranked in the order of CuO/CeO_2(S)-500 < CuO/CeO_2(C)-500 < CuO/CeO_2(N)-500 < CuO/CeO_2(A)-500, in agreement with the result of CO-TPD analysis described above.

3.9 Catalytic activity for CO oxidation

The activity data for different CuO/CeO_2 catalysts for CO oxidation are shown in Fig. 11. The catalytic activity of either CuO (not shown here) or CeO_2 is quite low, but when CuO species are introduced on the CeO_2 surface, the activity increases dramatically. This phenomenon may be mainly attributed to the improved CuO dispersion and the CuO–CeO_2 interaction resulting from the incorporation of a little bit of Cu^{2+} into the CeO_2 lattice and the stronger synergistic effects. Upon calcination at 500 °C, the catalytic activity of different catalysts increases in the order of CuO/CeO_2(S)-500 < CeO_2 < CuO/CeO_2(C)-500 < CuO/CeO_2(N)-500 < CuO/CeO_2(A)-500, consistent with the strength of the synergistic effects reflected in Raman, H_2-TPR, and DRIFTS analyses. This phenomenon suggests that synergistic effects play an important role in the activity process of CO oxidation. More specifically, the T_{99} (the temperature at which 99% CO conversion) for CuO/CeO_2(A)-500 is 117 °C, while the CO conversion on CuO/CeO_2(S)-500 is only 92.5% even when the reaction temperature reaches 500 °C. This result indicates that the catalytic activities are extremely sensitive to Cu precursors, from which different compositions and dispersions are obtained as shown in TG-DSC, XRD and Raman analyses. As a result, catalysts possessing different active sites and physicochemical properties exhibit disparate ability for CO oxidation.

The mechanism of conversion of CO to CO_2 on CuO/CeO_2 catalyst has been proposed to involve a redox cycle,[5,10,24,28] as shown in Scheme 1. At first, CO adsorbs on the active CuO species, mainly on Cu^+. In step 2, the adsorbed CO reacts with lattice oxygen giving rise to CO_2, accompanied by the formation of surface oxygen vacancies, Ce^{3+} and active adsorption sites Cu^+. The oxygen vacancies are replenished by gas-phase oxygen, leading to the re-oxidation of Cu^+ and Ce^{3+} in step 3. According to this reaction mechanism, it can be surmised that the highest activity observed for CuO/CeO_2-(A)-500 may be related to more highly dispersed active CuO (shown clearly in H_2-TPR analysis) and stronger synergistic

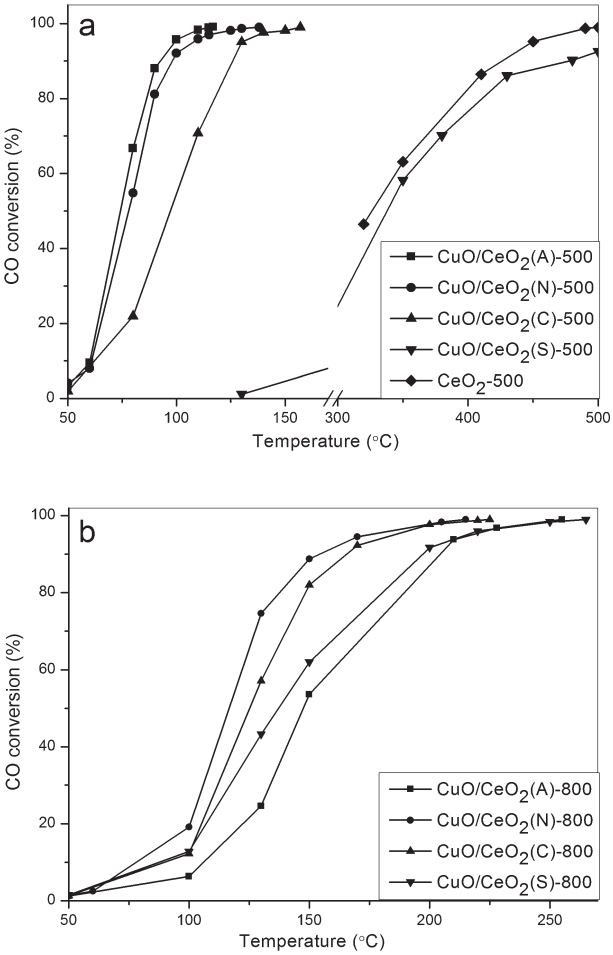

Fig. 11 Effect of Cu precursors on CO oxidation activity over CuO/CeO_2 catalysts calcined at 500 °C (a) and 800 °C (b).

effects between CuO and CeO_2 (reflected in Raman, H_2-TPR, and DRIFTS analyses); the former provides the sites for adsorbing CO and promotes the incorporation of Cu^{2+} into the CeO_2 lattice resulting in the formation of Ce^{3+} and oxygen vacancies, and the latter produces better CO adsorption sites Cu^+ and activates the lattice oxygen. In addition, the improved dispersion of CuO is also beneficial to strengthen the synergistic effects. This can be seen clearly from the results of CuO/CeO_2(A)-500 and CuO/CeO_2(N)-500, on which the differences in synergistic effects and activity for CO

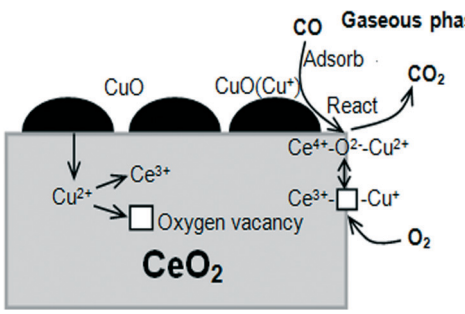

Scheme 1 Reaction models of CO oxidation over CuO/CeO_2 catalyst.

oxidation originate directly from the different dispersion of CuO. CuO/CeO_2(A)-500 with more highly dispersed CuO possesses stronger synergistic effects. Although CuO/CeO_2(C)-500 also has numerous highly dispersed Cu species, oxygen vacancies, Ce^{3+} and reduction degree of Cu^+, it shows a lower activity than CuO/CeO_2(A)-500 and CuO/CeO_2(N)-500. This can be ascribed to the presence of $Cu_2(OH)_3Cl$ and Cl^-: the former leads to a decreased amount of active CuO, while the latter inhibits the synergistic effects, making the activation of adsorbed CO and lattice oxygen more difficult. So, step 2 in the reaction process has been blocked. The catalytic activity of CuO/CeO_2(S)-500 with highly dispersed $CuSO_4$ and more Ce^{3+} is even lower than that of CeO_2 (Fig. 11a), probably because the presence of SO_4^{2-} completely interdicts the synergistic effects and makes the formation of better CO adsorption sites Cu^+ and the activation of lattice oxygen impossible at low temperature as reflected in CO-TPD and DRIFTS measurements.

Upon calcination at 800 °C, the catalytic activities of CuO/CeO_2 prepared from different Cu precursors increase in the following order: CuO/CeO_2(A)-800 < CuO/CeO_2(S)-800 < CuO/CeO_2(C)-800 < CuO/CeO_2(N)-800. Compared with the counterparts calcined at 500 °C, the catalytic activities of all CuO/CeO_2 catalysts except for CuO/CeO_2(S)-800 decrease obviously due to the sintering of both CuO and CeO_2. According to the literature, highly dispersed CuO shows a significantly higher activity for CO oxidation than the bulk CuO.[2,28,68,69] Thus, the sintering of highly dispersed CuO into bulk CuO leads to the formation of less active catalysts. On the contrary, CuO/CeO_2(S)-800 shows a higher activity than CuO/CeO_2(S)-500, due to the complete conversion of inactive $CuSO_4$ to CuO. What is more, the activity of CuO/CeO_2(S)-800 with largest CuO particles is higher than that of CuO/CeO_2-(A)-800; it may be related to the larger CeO_2 particles on CuO/CeO_2(A)-800. It is worth noting that CuO/CeO_2(A)-800 shows the lowest activity, while the highest activity is obtained on CuO/CeO_2(A)-500, suggesting that the active Cu species and CeO_2 on CuO/CeO_2(A) are less stable as the temperature increases. Moreover, CuO/CeO_2(C)-800 with a relatively lower Cu content (as shown in Table 1) shows a similar catalytic activity with CuO/CeO_2(N)-800, further suggesting that the redundant bulk CuO species only have a little contribution to the catalytic activity.[2,28,53,68–70]

4. Conclusions

The effects of Cu precursors (used in impregnation) and calcination temperatures on the physicochemical properties and catalytic activities of CuO/CeO_2 catalysts in CO oxidation were investigated in detail. When the samples are calcined at 500 °C, CuO is the dominant Cu species. The only exception is that for CuO/CeO_2(S)-500, in which $CuSO_4$ is dominant instead. CuO/CeO_2(A)-500 prepared using copper acetate shows the highest activity due to the better dispersion of CuO as well as enhanced CuO–CeO_2 synergistic effects. The stronger synergistic effects can lead to the reduction of CuO to Cu^+ species, which have better CO adsorptive properties and make the lattice oxygen more active, playing an important role in the improvement of the reducibility and activity for CO oxidation. The increased number of highly dispersed CuO can provide active CO adsorption sites (Cu^+ species) and strengthen the synergistic effects. However, the synergistic effects are significantly affected by the residual anions. The presence of Cl^- and SO_4^{2-} inhibits the synergistic effect, leading to a reduced activity. Comparing with CuO/CeO_2(A)-500, the CuO species on CuO/CeO_2(N)-500 prefers to aggregate on the CeO_2 surface, and the redundant bulk CuO species have almost no interaction with CeO_2 and contribute little to catalytic activity. On the other hand, the formation of oxygen vacancies and Ce^{3+} caused by the incorporation of Cu^{2+} into the CeO_2 lattice is predominantly affected by the disparity of Cu species: the more highly dispersed Cu species are, the more oxygen vacancies and Ce^{3+} are produced. The incorporation of Cu^{2+} into the CeO_2 lattice changes its lattice parameters (determined by XRD) by inducing the lattice to distort. In addition, the strong interaction between CuO and CeO_2 also has a significant influence on the structure of CeO_2, as reflected by the main F_{2g} mode band observed by Raman spectroscopy.

Upon calcination at 800 °C, the Cu species obtained from all Cu precursors are basically bulk CuO, which shows a little activity. So, the catalytic activities of these catalysts are significantly lower than those calcined at 500 °C, except that CuO/CeO_2(S)-800 is even more active than CuO/CeO_2(S)-500 due to the formation of CuO from the decomposition of inactive $CuSO_4$ and the elimination of site-blocking SO_4^{2-} species. CuO/CeO_2(C)-800 with lower Cu content shows better catalytic activity than CuO/CeO_2(A)-800 and CuO/CeO_2(S)-800 further demonstrating that the bulk CuO has only a little contribution to the catalytic activity.

Acknowledgements

This project was financially supported by the National Natural Science Foundation of China (21273150) and the "ShuGuang" Project (10GG23) of Shanghai Municipal Education Commission and Shanghai Education Development Foundation.

Notes and references

1 W. Liu and M. Flytzani-Stephanopoulos, *J. Catal.*, 1995, **153**, 304.
2 M. F. Luo, Y. J. Zhong, X. X. Yuan and X. M. Zheng, *Appl. Catal., A*, 1997, **162**, 121.
3 A. Tschöpe, D. Schaadt, R. Birringer and J. Y. Ying, *Nanostruct. Mater.*, 1997, **9**, 423.
4 X. Y. Jiang, G. L. Lu, R. X. Zhou, J. X. Mao, Y. Chen and X. M. Zheng, *Appl. Surf. Sci.*, 2001, **173**, 208.
5 G. Sedmak, S. Hočevar and J. Levec, *J. Catal.*, 2004, **222**, 87.
6 X. L. Tang, B. C. Zhang, Y. Li, Y. D. Xu, Q. Xin and W. J. Shen, *Catal. Today*, 2004, **93–95**, 191.
7 A. Martínez-Arias, A. B. Hungría, M. Fernández-García, J. C. Conesa and G. Munuera, *J. Phys. Chem. B*, 2004, **108**, 17983.

8 X. C. Zheng, S. H. Wu, S. P. Wang, S. R. Wang, S. M. Zhang and W. P. Huang, *Appl. Catal., A*, 2005, **283**, 217.
9 M. F. Luo, J. M. Ma, J. Q. Lu, Y. P. Song and Y. J. Wang, *J. Catal.*, 2007, **246**, 52.
10 L. Qi, Q. Yu, Y. Dai, C. J. Tang, L. J. Liu, H. L. Zhang, F. Gao, L. Dong and Y. Chen, *Appl. Catal., B*, 2012, **119–120**, 308.
11 F. Zhang, C. Chen, W. M. Xiao, L. Xu and N. Zhang, *Catal. Commun.*, 2012, **26**, 25.
12 D. S. Mao, L. H. Tao, Q. Wang, Y. L. Guo and G. Z. Lu, *Chin. J. Inorg. Chem.*, 2010, **26**, 447.
13 G. Avgouropoulos, T. Ioannides and H. Matralis, *Appl. Catal., B*, 2005, **56**, 87.
14 J. Li, Y. X. Han, Y. H. Zhu and R. X. Zhou, *Appl. Catal., B*, 2011, **108–109**, 72.
15 D. Gamarra, A. López Cámara, M. Monte, S. B. Rasmussen, L. E. Chinchilla, A. B. Hungría, G. Munuera, N. Gyorffy, Z. Schay, V. Cortés Corberán, J. C. Conesa and A. Martínez-Arias, *Appl. Catal., B*, 2013, **130–131**, 224.
16 C. R. Jung, J. Han, S. W. Nam, T. H. Lim, S. A. Hong and H. I. Lee, *Catal. Today*, 2004, **93–95**, 183.
17 D. Gamarra and A. Martínez-Arias, *J. Catal.*, 2009, **263**, 189.
18 A. C. Ferreira, A. M. Ferraria, A. M. B. do Rego, A. P. Gonçalves, A. V. Girão, R. Correia, T. A. Gasche and J. B. Branco, *J. Mol. Catal. A: Chem.*, 2010, **320**, 47.
19 C. Q. Hua, Q. S. Zhu, Z. Jiang, Y. Y. Zhang and Y. Wang, *Microporous Mesoporous Mater.*, 2008, **113**, 427.
20 D. Delimaris and T. Ioannides, *Appl. Catal., B*, 2009, **89**, 295.
21 L. J. Liu, J. G. Cai, L. Qi, Q. Yu, K. Q. Sun, B. Liu, F. Gao, L. Dong and Y. Chen, *J. Mol. Catal. A: Chem.*, 2010, **327**, 1.
22 P. Djinović, J. Batista and A. Pintar, *Appl. Catal., A*, 2008, **347**, 23.
23 R. Si, J. Raitano, N. Yi, L. H. Zhang, S. W. Chan and M. Flytzani-Stephanopoulos, *Catal. Today*, 2012, **180**, 68.
24 A. P. Jia, G. S. Hu, L. Meng, Y. L. Xie, J. Q. Lu and M. F. Luo, *J. Catal.*, 2012, **289**, 199.
25 A. Pintar, J. Batista and S. Hočevar, *J. Colloid Interface Sci.*, 2005, **285**, 218.
26 Z. Q. Yang, D. S. Mao, Q. S. Guo and L. Gu, *Acta Phys.-Chim. Sin.*, 2010, **26**, 3278.
27 S. M. Zhang, W. P. Huang, X. H. Qiu, B. Q. Li, X. C. Zheng and S. H. Wu, *Catal. Lett.*, 2002, **80**, 41.
28 Y. Liu, C. Wen, Y. Guo, G. Z. Lu and Y. Q. Wang, *J. Phys. Chem. C*, 2010, **114**, 9889.
29 J. W. Qin, J. F. Lu, M. H. Cao and C. W. Hu, *Nanoscale*, 2010, **2**, 2739.
30 M. Manzoli, R. Di Monte, F. Boccuzzi, S. Coluccia and J. Kašpar, *Appl. Catal., B*, 2005, **61**, 192.
31 X. C. Zheng, S. P. Wang, S. R. Wang, S. M. Zhang, W. P. Huang and S. H. Wu, *Catal. Commun.*, 2004, **5**, 729.
32 X. C. Zheng, X. L. Zhang, X. Y. Wang, S. R. Wang and S. H. Wu, *Appl. Catal., A*, 2005, **295**, 142.
33 E. D. Park and J. S. Lee, *J. Catal.*, 1998, **180**, 123.
34 C. Y. Lu, M. Y. Wey and Y. H. Fu, *Appl. Catal., A*, 2008, **344**, 36.
35 F. Wang and G. X. Lu, *Int. J. Hydrogen Energy*, 2010, **35**, 7253.
36 S. Espositoa, M. Turco, G. Bagnasco, C. Cammarano and P. Pernice, *Appl. Catal., A*, 2011, **403**, 128.
37 K. L. Zhang, J. H. Hong, G. H. Cao, D. Zhan, Y. T. Tao and C. J. Cong, *Thermochim. Acta*, 2005, **437**, 145.
38 T. Cseri, S. Békássy, G. Kenessey, G. Liptay and F. Figueras, *Thermochim. Acta*, 1996, **288**, 137.
39 I. V. Morozov, K. O. Znamenkov, Y. M. Korenev and O. A. Shlyakhtin, *Thermochim. Acta*, 2003, **403**, 173.
40 K. D. Kim, I. S. Nam, J. S. Chung, J. S. Lee, S. G. Ryu and Y. S. Yang, *Appl. Catal., B*, 1994, **5**, 103.
41 J. S. Lee, S. H. Choi, K. D. Kim and M. Nomura, *Appl. Catal., B*, 1996, **7**, 199.
42 S. Hoffmann, M. Schmidt, S. Scharsach and R. Kniep, *Thermochim. Acta*, 2012, **527**, 204.
43 Z. Li, R. Y. Wang, H. Y. Zheng and K. C. Xie, *Fuel*, 2010, **89**, 1339.
44 A. Saig, A. Danon, Y. Finkelstein, G. Kimmel and J. E. Koresh, *J. Phys. Chem. Solids*, 2003, **64**, 701.
45 M. Olszak-Humienik and J. Możejko, *Thermochim. Acta*, 2003, **405**, 171.
46 Z. Zhang, X. B. Ma, P. B. Zhang, Y. M. Li and S. P. Wang, *J. Mol. Catal. A: Chem.*, 2007, **266**, 202.
47 F. Fajardie, J. F. Tempere, J. M. Manoli, G. Djega-Mariadassou and G. Blanchardb, *J. Chem. Soc., Faraday Trans.*, 1998, **94**, 3727.
48 M. Fernández-García, A. Martínez-Arias, A. Iglesias-Juez, C. Belver, A. B. Hungría, J. C. Conesa and J. Soria, *J. Catal.*, 2000, **194**, 385.
49 J. R. McBride, K. C. Hass, B. D. Poindexter and W. H. Weber, *J. Appl. Phys.*, 1994, **76**, 2435.
50 L. Kuang, P. Huang, H. H. Sun, H. X. Jiang and M. H. Zhang, *J. Rare Earths*, 2013, **31**, 137.
51 B. M. Reddy and A. Khan, *Catal. Surv. Asia*, 2005, **9**, 155.
52 S. P. Wang, X. Y. Wang, J. Huang, S. M. Zhang, S. R. Wang and S. H. Wu, *Catal. Commun.*, 2007, **8**, 231.
53 L. Ilieva, G. Pantaleo, I. Ivanov, A. M. Venezia and D. Andreeva, *Appl. Catal., B*, 2006, **65**, 101.
54 J. Silvestre-Albero, F. Rodríguez-Reinoso and A. Sepúlveda-Escribano, *J. Catal.*, 2002, **210**, 127.
55 W. D. Cai, F. Chen, X. X. Shen, L. J. Chen and J. L. Zhang, *Appl. Catal., B*, 2010, **101**, 160.
56 P. Zimmer, A. Tschöpe and R. Birringer, *J. Catal.*, 2002, **205**, 339.
57 J. Liu, X. J. Lă, G. D. Zhou, K. J. Zhen, W. X. Zhang and T. X. Cheng, *React. Kinet. Catal. Lett.*, 2006, **88**, 315.
58 Y. X. Shen, G. Z. Lu, Y. Guo, Y. Q. Wang, Y. L. Guo and X. Q. Gong, *Catal. Today*, 2011, **175**, 558.
59 M. Abid, G. Ehret and R. Touroude, *Appl. Catal., A*, 2001, **217**, 219.
60 T. Caputo, L. Lisi, R. Pirone and G. Russo, *Appl. Catal., A*, 2008, **348**, 42.
61 G. Avgouropoulos and T. Ioannides, *J. Mol. Catal. A: Chem.*, 2008, **296**, 47.
62 S. M. Ma, G. Z. Lu, Y. X. Shen, Y. Guo, Y. Q. Wang and Y. L. Guo, *Catal. Sci. Technol.*, 2011, **1**, 669.
63 A. Martínez-Arias, M. Fernández-García, O. Gálvez, J. M. Coronado, J. A. Anderson, J. C. Conesa, J. Soria and G. Munueraz, *J. Catal.*, 2000, **195**, 207.

64 A. Martínez-Arias, M. Fernández-García, J. Soria and J. C. Conesa, *J. Catal.*, 1999, **182**, 367.
65 P. Bera, A. L. Cámara, A. Hornés and A. Martínez-Arias, *J. Phys. Chem. C*, 2009, **113**, 10689.
66 D. Scarano, S. Bordiga, C. Lamberti, G. Spoto, G. Ricchiardi, A. Zecchina and C. Otero Areán, *Surf. Sci.*, 1998, **411**, 272.
67 C. Binet, M. Daturi and J. C. Lavalley, *Catal. Today*, 1999, **50**, 207.
68 M. F. Luo, Y. P. Song, J. Q. Lu, X. Y. Wang and Z. Y. Pu, *J. Phys. Chem. C*, 2007, **111**, 12686.
69 G. Aguila, S. Guerrero and P. Araya, *Appl. Catal., A*, 2013, **462–463**, 56.
70 Z. Q. Yang, D. S. Mao, X. M. Guo and G. Z. Lu, *J. Rare Earths*, 2014, **32**, 117.